https://doi.org/10.5194/egusphere-2026-4148
Preprint. Discussion started: 31 July 2026

Spectral analysis of GNSS zenith wet delay and microwave radiometer precipitable water during FESSTVaL Lindenberg 2021: a multi-scale observational test of horizontal heterogeneity sensitivity

Gaël Kermarrec[1,2], Xavier Calbet[3], Nishant Pawar[1], and Zhiguo Deng[4]

[1]Institute of Meteorology and Climatology, Leibniz Universität Hannover, Hannover, Germany
[2]GEO-NET Umweltconsulting GmbH, Hannover, Germany
[3]Agencia Estatal de Meteorología (AEMET), Madrid, Spain
[4]GFZ Helmholtz Centre for Geosciences, Space Geodetic Techniques, Potsdam, Germany

Correspondence: Gaël Kermarrec (kermarrec@meteo.uni-hannover.de)

Abstract. Every Global Navigation Satellite System (GNSS) station estimates a zenith wet delay (ZWD), a direct measure of the water vapour integrated above it. The ZWD is a standard product of GNSS meteorology, yet its small-scale temporal structure is conventionally treated as noise. We ask whether the temporal spectrum of the ZWD reveals horizontal water vapour heterogeneity near the boundary layer top that a vertical sounding cannot see. Using FESSTVaL observations at Lindenberg in summer 2021, we compare the GNSS ZWD with the precipitable water from a microwave radiometer over 28 days. Both are described by a Matérn spectrum whose scale and amplitude are tracked on sliding windows. The radiometer scale follows the boundary layer height in calm conditions and shifts to a wind-driven, advective behaviour when the atmosphere becomes unstable, confirmed by tower turbulence. The GNSS scale stays stable across all conditions, because its oblique geometry ties it to horizontal structure at the boundary layer top, unchanged by the shifts in vertical stability. The strength of the GNSS signal grows with the horizontal heterogeneity measured independently at two scales ($\rho = +0.433$ and $+0.525$), while the vertical radiometer shows none and a scintillometer rules out a surface contribution. Accessible from any positioning solution, the GNSS scale measures horizontal coherence at the boundary layer top that is far more stable than the ERA5 boundary layer height (coefficient of variation 0.32 against 0.90) and persists through the night.

1 Introduction

Water vapour is the most variable constituent of the atmospheric boundary layer (BL), fluctuating from the turbulent scale up to the sub-mesoscale. These fluctuations partly control where moist convection is triggered (Hohenegger et al., 2023). Water vapour also delays the microwave signals of Global Navigation Satellite System (GNSS) receivers, in proportion to the amount along the path. GNSS meteorology turns this delay, the zenith wet delay (ZWD), into the total column of water vapour over each station (Bevis et al., 1992). That column is a slowly varying, bulk quantity, and it is now standard input to forecasting and reanalysis. The fine temporal structure of the ZWD is discarded as noise.

https://doi.org/10.5194/egusphere-2026-4148
Preprint. Discussion started: 31 July 2026

The temporal spectrum of the ZWD has recently been shown to carry information about BL turbulence (Kermarrec et al., 2025; Kermarrec, 2024). The ZWD also carries spatial information. Each satellite is observed at an angle, so the delay along its line of sight samples water vapour to the side as well as overhead. The ZWD mixes vertical and horizontal structure, whereas a zenith-pointing microwave radiometer (MWR) sounds a single vertical column.

The slant geometry's horizontal content is not a new idea. Horizontal gradients estimated jointly with the ZWD have long captured the azimuthal asymmetry of the wet delay (Chen and Herring, 1997), and water vapour tomography reconstructs three-dimensional humidity fields from dense networks of slant delays (Flores et al., 2000; Champollion et al., 2005; Bender et al., 2011). A spectral approach goes further. The second-order structure of a single-station ZWD, summarised by the scale λ_{ZWD} of a Matérn fit, carries information about horizontal coherence on its own, without the dense network of tomography or the gradient fitted in routine processing. The GNSS ZWD spectrum should respond to horizontal water vapour heterogeneity at the BL top that a vertical sounding cannot resolve, a hypothesis that can be tested against collocated heterogeneity measurements. Testing it requires a site where the GNSS signal can be compared with independent measurements of that heterogeneity at several spatial scales at once.

The Field Experiment on Sub-mesoscale Spatio-Temporal Variability in Lindenberg (FESSTVaL, Hohenegger et al., 2023) offers such a site. Lindenberg already operates a permanent GNSS station, a zenith MWR, an optical-microwave scintillometer over a 4.85 km path and operational radiosondes. For the summer 2021 intensive observation period, FESSTVaL deployed an azimuth-scanning MWR (FOGHAT) at Lindenberg and two further MWRs at the Falkenberg and Birkholz supersites 5–6 km away. This collocated density allows a direct, multi-scale test of whether the GNSS ZWD spectrum sees horizontal structure that vertical MWR sounding misses.

Several questions follow, and no single instrument can settle them. Does the GNSS spectral scale respond to horizontal heterogeneity that a vertical sounding cannot see, or does it merely follow the depth of the BL? How does its behaviour differ from that of the vertical radiometer as the atmosphere moves from calm to weakly unstable conditions? In the vertical, where does the variance seen by GNSS but not by the radiometer originate? And once treated as a standalone observable, does the GNSS scale carry information that the reanalysis boundary layer height (BLH) does not? The triangle of three zenith radiometers 5–6 km apart is central to answering them: it provides a direct measurement of the horizontal heterogeneity against which the coherence carried by λ_{ZWD} can be anchored. This turns the interpretation of the GNSS spectral scale from an inference into a testable comparison.

Here we fit Matérn spectra to the GNSS ZWD and the MWR Precipitable Water (PRW) on 62.5 min sliding windows over the 28-day period. We then attribute the fitted parameters to physical drivers using the FESSTVaL auxiliary instruments, with ERA5 and the operational radiosondes as the reference BLH. If the GNSS spectrum resolves this heterogeneity, a quantity already produced operationally at thousands of stations would deliver, in all weather and through the diurnal cycle, a measure of horizontal water vapour structure at the BL top that neither vertical sounding nor reanalysis provides.

The paper is organised as follows. Section 2 describes the Lindenberg site and the FESSTVaL instruments. Section 3 sets out the Matérn spectral fit, the construction of the excess GNSS variance σ_{extra}, and the driver analysis. Section 4 takes up these

https://doi.org/10.5194/egusphere-2026-4148
Preprint. Discussion started: 31 July 2026

questions in turn. Section 5 interprets them through the measurement geometry, and Section 6 summarises the findings and points to extensions.

2 Data

2.1 Site

The Meteorological Observatory Lindenberg, Richard Aßmann Observatory (MOL-RAO) is operated by the German Weather Service (DWD) near Berlin (52.21°N, 14.12°E, 73 m above sea level). It hosts an operational measurement program including radiosondes, MWRs, Doppler lidars, cloud radars, ceilometers, scintillometers, and a baseline surface radiation station. The FESSTVaL campaign (Hohenegger et al., 2023) added a hierarchical observation strategy during summer 2021. Three supersites (Lindenberg, Falkenberg, Birkholz) form a triangle of edge length 5–6 km. A dense network of low-cost surface stations within a 15 km radius around the BL field site GM Falkenberg resolves submesoscale phenomena such as cold pools and wind gusts at the hectometre to kilometre scale (Kirsch et al., 2022a). Figure 1 shows the triangle geometry and the location in Brandenburg, and Fig. 2 the site and its main instruments.

The intensive observation period (IOP) ran from 5 June to 5 July 2021, with the special observation period (SOP) starting 7 June. Our analysis window spans 28 days from 7 June to 4 July 2021. It covers the full IOP minus the first 48 hours of settling.

2.2 GNSS ZWD from PRIDE PPP

The Lindenberg site hosts the International GNSS Service (IGS) station LDB2 (Trimble NETR9 receiver, choke ring antenna). RINEX observations were processed with the precise point positioning (PPP) software PRIDE PPP-AR (Geng et al., 2019) using IGS final orbits and clocks, to produce ZWD at 30 s cadence. At each epoch the software outputs the zenith hydrostatic delay, an a priori ZWD, and a corrected ZWD (ZWDcor) that accounts for residual mapping-function errors and tropospheric gradients. We use ZWDcor as the primary observable. At 30 s cadence, each 62.5 min spectral window contains up to 125 samples, sufficient to resolve the spectral slope and the saturation scale of the Matérn process (Section 3.1). The companion station LIN0 is reprocessed in the same way for differential analysis. Its data quality is inferior to LDB2 because of the antenna environment, so LIN0 serves only as a differential proxy for constellation geometry effects.

2.3 MWR PRW from HATPRO RAOHAT

The HATPRO (Humidity and Temperature Profiler) MWR RAOHAT (Rose et al., 2005), operated by DWD at the Lindenberg site, provides brightness temperatures in 7 K-band channels (22 to 32 GHz) and 7 V-band channels (51 to 58 GHz), with a cadence of approximately 2 seconds. The PRW is retrieved from the K-band channels with a manufacturer specified accuracy of order 0.5 $\mathrm{kg\,m^{-2}}$. Throughout this analysis, we convert PRW (in $\mathrm{kg\,m^{-2}}$) to its ZWD equivalent $\mathrm{PRW_{eq}}$ using the Bevis mapping coefficient (Bevis et al., 1992, 1994)

https://doi.org/10.5194/egusphere-2026-4148
Preprint. Discussion started: 31 July 2026

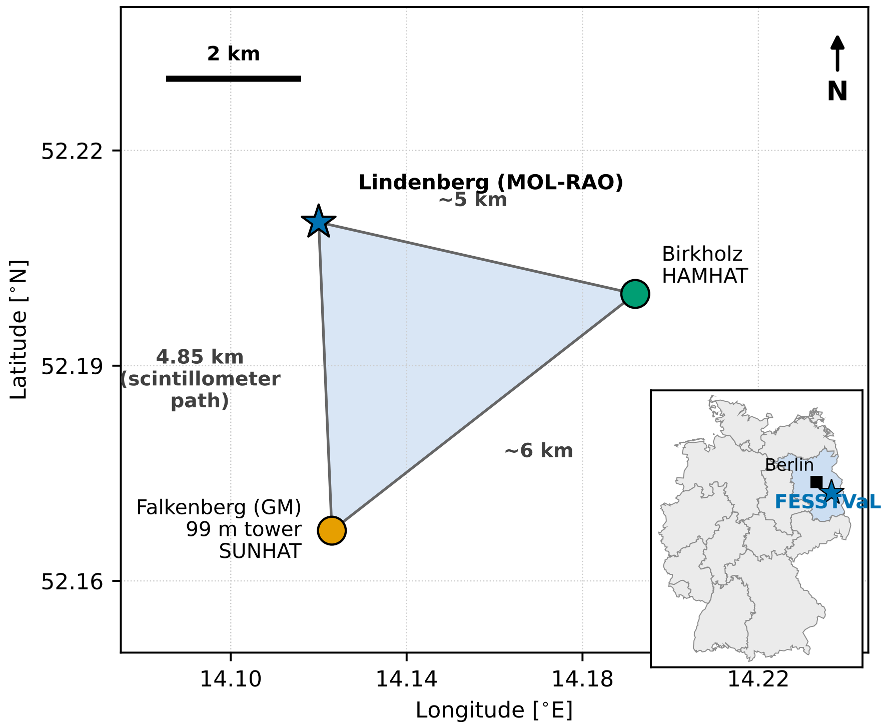

Figure 1. The FESSTVaL supersites near Lindenberg. The GNSS station LDB2, with the radiometers RAOHAT and FOGHAT, is at the Lindenberg MOL-RAO site; SUNHAT and the 99 m turbulence tower are at Falkenberg (GM); HAMHAT is at Birkholz. Dashed lines give the inter-site distances, and the Lindenberg–Falkenberg baseline coincides with the 4.85 km scintillometer path. The inset locates the site in Brandenburg, southeast of Berlin.

$$\Pi = \frac{10^6}{\rho_w R_v \left(k_3/T_m + k_2'\right)} \approx 6.46 \text{ mm of ZWD per kg m}^{-2} \text{ of PRW,} \quad (1)$$

at the local mean temperature T_m. This conversion allows direct spectral comparison of variances between MWR and GNSS in homogeneous units. The radiometer follows standard zenith observation interrupted every 10 minutes by elevation scans for temperature profile retrieval (Crewell and Löhnert, 2007). Ground-based microwave radiometry of this type provides continuous thermodynamic profiling that complements the operational radiosondes (Löhnert and Maier, 2012; Turner and Löhnert, 2021).

2.4 Falkenberg tower turbulence

The BL field site GM Falkenberg is located 4.85 km south of Lindenberg. It hosts a 99 m meteorological mast with eddy covariance measurements at 50.3 m and 90.3 m (Metek USA1 sonic anemometer and Licor LI7500 hygrometer at 20 Hz). The associated turbulence parameters (turbulent kinetic energy TKE, friction velocity u_*, the vertical fluxes of sensible heat, latent

https://doi.org/10.5194/egusphere-2026-4148
Preprint. Discussion started: 31 July 2026

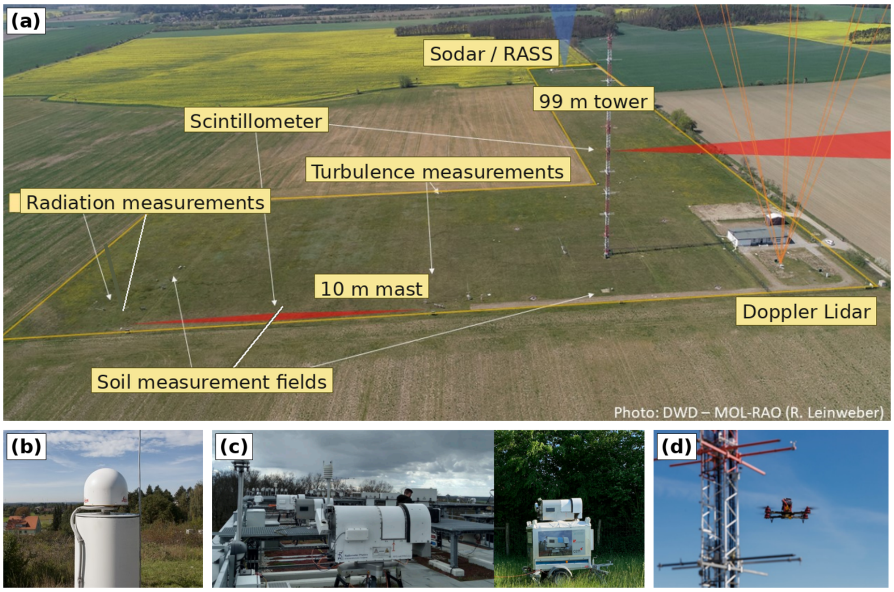

Figure 2. The FESSTVaL site and instrumentation. (a) The GM Falkenberg BL field site with the 99 m tower, 10 m mast, scintillometer path, and turbulence, radiation and soil measurements (photo: DWD MOL-RAO, R. Leinweber). (b) The LDB2 GNSS antenna at Lindenberg. (c) The MWR profilers FOGHAT, SUNHAT and RAOHAT during the common calibration at Lindenberg on 3 May 2021 (left) and HAMHAT at Birkholz (right). (d) The Falkenberg 99 m tower. Photos courtesy of DWD MOL-RAO (Hohenegger et al., 2023).

heat and water vapour, and similarity scales) are computed at 30 min resolution and are available through Frank Beyrich on the FDR Hamburg repository (Beyrich, 2024, DOI 10.25592/uhhfdm.14239). For this analysis, we use the 30 min turbulence file at level 2 (90.3 m), the 99 m tower profile of wind speed, and the surface basic meteorology including downward fluxes. Quality control follows the principles described in Beyrich and Adam (2007).

2.5 ERA5 reanalysis

ERA5 hourly instantaneous fields (Hersbach et al., 2020) are extracted at the Lindenberg grid point (52.21°N, 14.12°E) for the analysis window: BLH, total column water vapour (TCWV), 10 m wind components (U10, V10), convective available potential energy (CAPE), and K-index (KX). The ERA5 BLH is computed by the European Centre for Medium-Range Weather Forecasts (ECMWF) following the Richardson bulk number approach and provides our baseline reference for BL scale. Variables are interpolated onto the 5 min analysis grid.

2.6 Operational radiosondes

DWD operates radiosondes at MOL-RAO at 04:45, 10:45, 16:45, and 22:45 UTC. The FESSTVaL campaign added experimental launches on days with thunderstorm forecasts or special operations. For the boundary-layer scale comparison in Sec-

https://doi.org/10.5194/egusphere-2026-4148
Preprint. Discussion started: 31 July 2026

tion 4.4, we use 101 good-quality (Q=G) soundings from the 28-day window for which the operational mixing-layer height converged. This operational BLH is derived by DWD MOL-RAO from the routine radiosoundings following the method of Beyrich and Leps (2012), based on inversion detection and the bulk Richardson number, and was provided by DWD MOL-RAO (F. Beyrich, personal communication, 2026). For comparison we also computed BLH with a parcel method (Seidel et al., 2010), $\mathrm{BLH} = \min\{z > 150\,\mathrm{m} : \theta_v(z) \geq \theta_v(\mathrm{surface}) + 1.5\,\mathrm{K}\}$, applied to the raw FESSTVaL radiosonde profiles from the ICDC repository (Kirsch et al., 2022b), on 113 ascents.

2.7 Auxiliary observations for direct validation

Three additional FESSTVaL data sets are used to directly validate the geometric interpretation of σ_{extra} and λ_{ZWD} (Section 4.5):

2.7.1 FOGHAT azimuth-scanning HATPRO

A second HATPRO operated by the University of Cologne (FOGHAT) on the Lindenberg radiation platform scans continuously through 0° to 360° in azimuth at a fixed 30° elevation. It retrieves the off-zenith integrated water vapour (IWV) $\mathrm{PRW}_{\mathrm{oz}}$ roughly every 2 s. Variable name in the Standardized Atmospheric Measurement Data (SAMD) level-2 product: `prw_off_zenith`. The azimuthal variance of $\mathrm{PRW}_{\mathrm{oz}}$ on 62.5 min windows constitutes a direct measurement of horizontal water vapour heterogeneity above the site, independent of GNSS. Because FOGHAT scans off-zenith at 30° elevation, each measurement integrates along a slant path. The resulting σ_{azi} quantifies azimuthal contrasts of the slant-integrated vapour column, which is the relevant comparison quantity for the oblique GNSS geometry rather than a strictly horizontal cut. Independent characterisation of sub-mesoscale water vapour variability at Lindenberg during FESSTVaL has also been obtained from a vertically-pointing water vapour differential absorption lidar (DIAL) (Speidel et al., 2025).

2.7.2 HAMHAT and SUNHAT supersite HATPROs

Two additional HATPRO MWRs provide zenith PRW at the FESSTVaL supersites: HAMHAT, operated by the University of Hamburg at Birkholz, Gut Hirschaue (52.200°N, 14.192°E, about 5 km distance to Lindenberg), and SUNHAT, operated by the University of Cologne at Falkenberg (52.167°N, 14.123°E, 4.85 km distance to Lindenberg). All three instruments retrieve the zenith IWV from their K-band channels; SUNHAT additionally runs continuous elevation scans for boundary-layer temperature profiling. Together with RAOHAT at Lindenberg, they form a triangle of MWR zenith PRW measurements at the supersites scale. This gives a direct test of inter-site coherence at 5–6 km. The zenith IWV retrieval uses the same HATPRO K-band channels and manufacturer algorithm at each site, so the inter-site differences reflect physical heterogeneity rather than retrieval artefacts. A dedicated FESSTVaL calibration campaign quantified the inter-instrument brightness temperature consistency of the FESSTVaL HATPROs, including FOGHAT (Böck et al., 2025).

https://doi.org/10.5194/egusphere-2026-4148
Preprint. Discussion started: 31 July 2026

2.7.3 Optical-microwave scintillometer and structure parameters

A BLS-900 large-aperture optical scintillometer and a MWSC-160 microwave scintillometer operated jointly across a 4.85 km path between the Falkenberg supersite and the Lindenberg observatory (Päschke et al., 2023), with an effective measurement height of approximately 43 m. We use three products derived from this instrument pair, made available by DWD MOL-RAO. First, the directly measured optical refractive index structure parameter $C_n^2(\mathrm{opt})$ from the BLS-900 at 10 min cadence (17712 values over the period, median 2.23×10^{-15} $\mathrm{m}^{-2/3}$). Second, the structure parameters of temperature C_T^2, of humidity C_q^2, and the temperature-humidity covariance C_{Tq}, obtained from the manufacturer Optical-Microwave Scintillometer (OMS) processing following Hill (1997), Lüdi et al. (2005) and Kooijmans and Hartogensis (2016) (13324 valid samples after removal of rain and saturation flags). Third, the published level-2 regional-scale sensible and latent heat fluxes (Päschke et al., 2023). From the structure parameters we reconstruct the microwave refractive index structure parameter $C_n^2(\mathrm{MW})$ relevant to the GNSS frequency band (Section 3.3). These products together provide independent surface-layer turbulence intensity estimates integrated over the 4.85 km path at 43 m height. They complement the Falkenberg tower point-sensor fluxes.

2.8 RADOLAN precipitation

The DWD RADOLAN radar composite at 1 km, 5 min resolution provides precipitation context for the analysis window. 18 precipitation events of various intensity are identified within the 28 days, used to filter out windows with non-turbulent rain contamination in the GNSS PPP.

3 Methodology

We reduce the two observables to spectral parameters and attribute those parameters to physical drivers. Each series is fitted with a Matérn spectrum. From the fits we form the excess variance σ_{extra} and the reconstructed structure parameter, and relate both to ERA5 and in situ drivers. Figure 3 summarises the pipeline.

3.1 Spectral fit of ZWD and PRW

Both ZWD and PRW time series are fitted on a Matérn isotropic spectrum

$$S(f) = \frac{A}{(\lambda^2 + (2\pi f)^2)^{\nu+1/2}}, \tag{2}$$

with smoothness parameter ν fixed at $5/6$, which sets the exponent to $\nu + 1/2 = 4/3$ and the high-frequency slope to $-8/3$, the von Kármán form for turbulent refractivity (Kermarrec and Schön, 2014; Lilly et al., 2017). Here λ is the inverse correlation time (units s^{-1}). The adequacy of the Matérn and von Kármán spectral form for integrated atmospheric refractivity, including above the BLH, was demonstrated on large eddy simulations (Kermarrec et al., 2026). The fit is performed by debiased Whittle

https://doi.org/10.5194/egusphere-2026-4148
Preprint. Discussion started: 31 July 2026

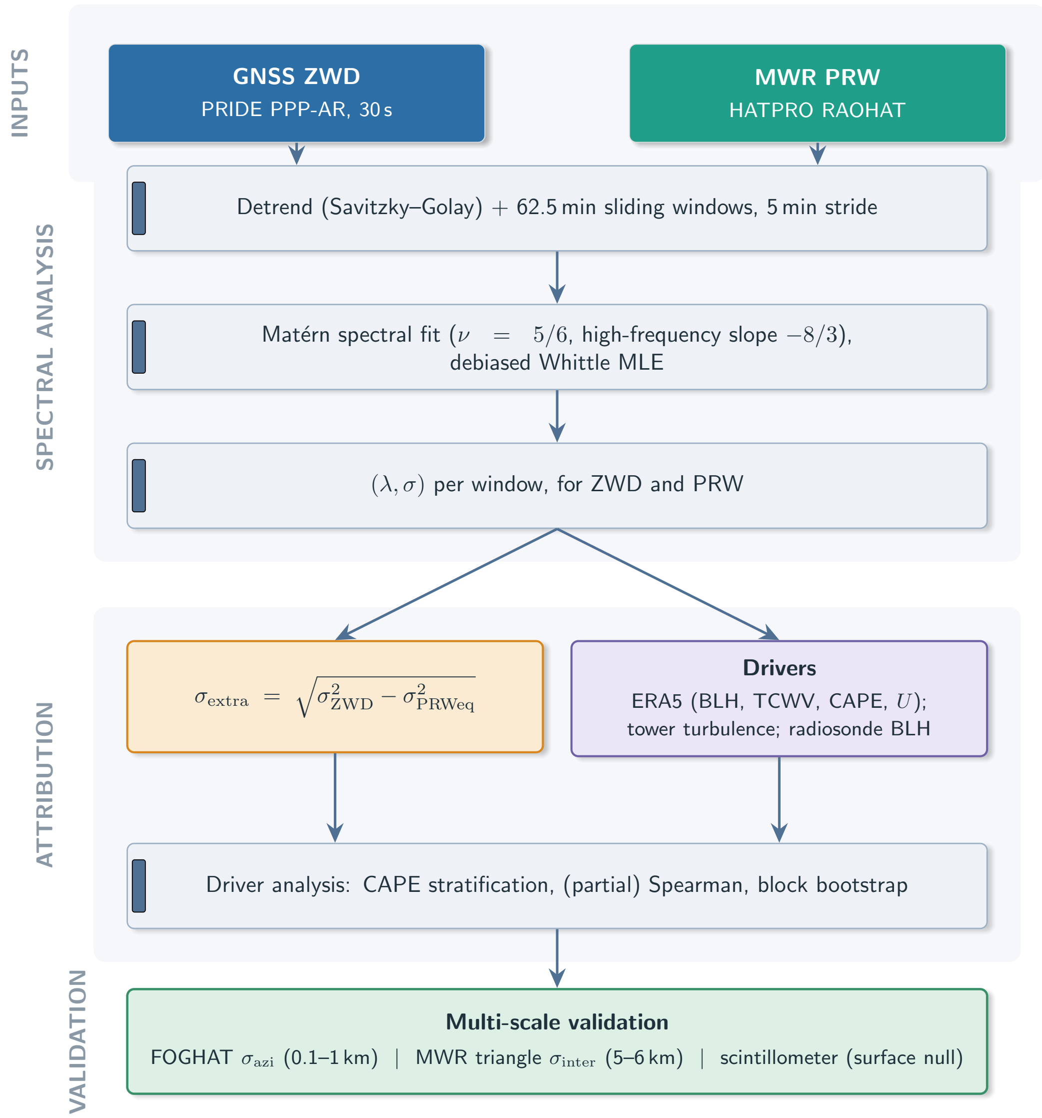

Figure 3. Overview of the processing pipeline. The two collocated observables, the GNSS ZWD and the MWR PRW, are reduced to Matérn spectral parameters (λ, σ) on 62.5 min sliding windows. The excess variance σ_{extra} and the fitted parameters are then attributed to physical drivers and validated against independent measurements of horizontal heterogeneity at two spatial scales, with a surface null control.

maximum likelihood estimation (Sykulski et al., 2019; Guillaumin et al., 2022) on sliding windows of 62.5 min duration with a stride of 5 minutes. For the 28-day analysis window, this produces 8001 Matérn spectral fits of (λ, σ^2) for each observable.

A pre-processing step removes deterministic trends using a Savitzky-Golay filter of length 25 min and order 2 (Kermarrec et al., 2025). This filter removes low frequency content below approximately $1/(25\ \mathrm{min})$ and preserves the high frequency

https://doi.org/10.5194/egusphere-2026-4148
Preprint. Discussion started: 31 July 2026

spectral signature targeted by the Matérn fit. The standard deviation σ extracted from the fit is the high frequency variability after detrending.

3.2 σ_{PRWeq} scaling and σ_{extra} construction

To enable a direct comparison of high frequency variability between GNSS and MWR, we apply the Bevis mapping coefficient $\Pi = 6.46\ \mathrm{mm\,kg^{-1}}$ to convert σ_{PRW} into its ZWD equivalent σ_{PRWeq}. The empirical ratio $\sigma_{\mathrm{ZWD}}/\sigma_{\mathrm{PRWeq}}$ is approximately 3.7 across the 28 days. We define the unexplained excess as

$$\sigma_{\mathrm{extra}} = \sqrt{\sigma_{\mathrm{ZWD}}^2 - \sigma_{\mathrm{PRWeq}}^2}, \tag{3}$$

which represents the high frequency variance present in the GNSS ZWD but absent from the MWR PRW. Because the difference under the square root can be negative on individual windows where σ_{PRWeq} exceeds σ_{ZWD} (typically when the MWR retrieval noise inflates the PRW spectral amplitude), σ_{extra} is set to zero on those windows. This occurs on about 7 percent of windows, given the empirical ratio $\sigma_{\mathrm{ZWD}}/\sigma_{\mathrm{PRWeq}} \approx 3.7$ that places most windows well away from the crossover, and the floored windows are retained in the correlation analyses so that no selection on the sign of the difference is introduced. The origin of this quantity is located in Section 4.3.

3.3 Microwave C_n^2 reconstruction from structure parameters

The microwave scintillometer is sensitive to the refractive index structure parameter C_n^2 at the MWSC-160 frequency near 11 GHz, dominated by water vapour fluctuations. From the OMS-derived temperature, humidity, and covariance structure parameters, we reconstruct $C_n^2(\mathrm{MW})$ following the standard refractivity decomposition (Hill, 1997; Ward et al., 2013)

$$C_n^2 = \left(\frac{\partial n}{\partial T}\right)^2 C_T^2 + 2\frac{\partial n}{\partial T}\frac{\partial n}{\partial q}C_{Tq} + \left(\frac{\partial n}{\partial q}\right)^2 C_q^2, \tag{4}$$

with the radio-frequency partial derivatives $\partial n/\partial q \approx +6\times10^{-4}$ per unit specific humidity and $\partial n/\partial T \approx -1\times10^{-6}\ \mathrm{K^{-1}}$ at 11 GHz. In this band the humidity term dominates by four orders of magnitude, so that $C_n^2(\mathrm{MW}) \approx (\partial n/\partial q)^2 C_q^2$. As an internal consistency check, we also reconstruct the optical $C_n^2(\mathrm{opt})$ from C_T^2 using the optical-frequency derivatives and compare it to the directly measured BLS-900 value; the two agree to within a factor of 1.14 (medians 2.55×10^{-15} versus $2.23\times10^{-15}\ \mathrm{m^{-2/3}}$); this confirms the structure-parameter to C_n^2 conversion. This reconstructed $C_n^2(\mathrm{MW})$ provides the most physically direct surface-layer turbulence proxy at the GNSS frequency band for the null test in Section 4.5.

3.4 Driver analysis and CAPE stratification

For each spectral-fit window, ERA5 drivers (BLH, U, V, CAPE, KX, TCWV) and turbulence variables from Falkenberg (TKE, u_*, sensible heat flux, w_*) are temporally aligned. Spearman rank correlations are computed between λ_{PRW}, λ_{ZWD}, σ_{PRW},

https://doi.org/10.5194/egusphere-2026-4148
Preprint. Discussion started: 31 July 2026

σ_{ZWD} and each driver. We then stratify by CAPE terciles (or 5 classes when sample size permits) to test the stability of these correlations across regimes. The highest CAPE tercile typically corresponds to values above about 20 J kg^{-1} in this summer 2021 window at Lindenberg. We stress that these are weakly unstable conditions in the absolute sense, far below the threshold for deep convection, and that the stratification is relative to the local summer 2021 CAPE distribution rather than to an absolute convective threshold.

A bootstrap of 1000 resamples on each stratification gives confidence intervals on the inter-regime differences $\Delta\rho$ and $\Delta\lambda$. Collinearity among the drivers is checked and found negligible, with variance inflation factors below 1.05.

3.5 In situ validation with Falkenberg turbulence

To validate the regime shift hypothesis on λ_{PRW}, the same CAPE stratification and Spearman correlations are computed between the spectral parameters and the in situ turbulence measurements at the 90 m level on the Falkenberg tower. Because turbulence variables are measured directly at 90 m without any modelling assumption, they constitute an independent test of the spectral signatures derived from radiometry and GNSS.

4 Results

We present the results in the order in which the questions were raised in the introduction. We first contrast the two spectral scales as the atmosphere moves from calm to weakly unstable conditions, then locate the origin of the excess GNSS variance in the vertical, examine λ_{ZWD} as a standalone observable, and finally test the horizontal-heterogeneity interpretation against the independent instruments.

4.1 Regime shift in λ_{PRW} between calm and weakly unstable conditions

Figure 4 gives an overview of the spectral parameters and the ERA5 drivers across the 28-day window. In calm conditions, λ_{PRW} correlates negatively with the ERA5 BLH, $\rho = -0.230$. This is the sign expected when the structures crossing the site have a characteristic length that scales with BLH. In the highest CAPE tercile (above about 20 J kg^{-1}, still weakly unstable in absolute terms), the correlation weakens to $\rho = -0.003$. The bootstrap with 1000 resamples gives $\Delta\rho = +0.227$ with 95 % confidence interval (CI95) $[+0.179, +0.274]$, so the change excludes zero on this dataset (Fig. 5).

Simultaneously, λ_{PRW} shifts towards a Taylor advective signature. In the highest CAPE tercile it correlates with the wind speed at half the BLH, $\rho(\lambda_{\mathrm{PRW}}, U_{BL/2}) = +0.330$, and the Taylor R^2 rises from 0.004 in CAPE class 1 (calm) to 0.137 in CAPE class 5 (weakly unstable). The joint regression of λ_{PRW} on U and shear in the high tercile yields a t statistic of $+17.2$ on $U_{BL/2}$, dominant over all other predictors. We note that a Taylor R^2 of 0.137 indicates that advection becomes the leading single predictor in this tercile, not that it explains most of the variance.

Independent validation comes from the Falkenberg turbulence at 90 m. The correlation $\rho(\lambda_{\mathrm{PRW}}, u_{*,90m})$ goes from -0.20 in the CAPE mid tercile to $+0.21$ in CAPE high, an in situ delta of $+0.41$ that mirrors the spectral result obtained from radiometry. The physical interpretation is that the weakly unstable regime organises structures whose length is less tied to

https://doi.org/10.5194/egusphere-2026-4148
Preprint. Discussion started: 31 July 2026

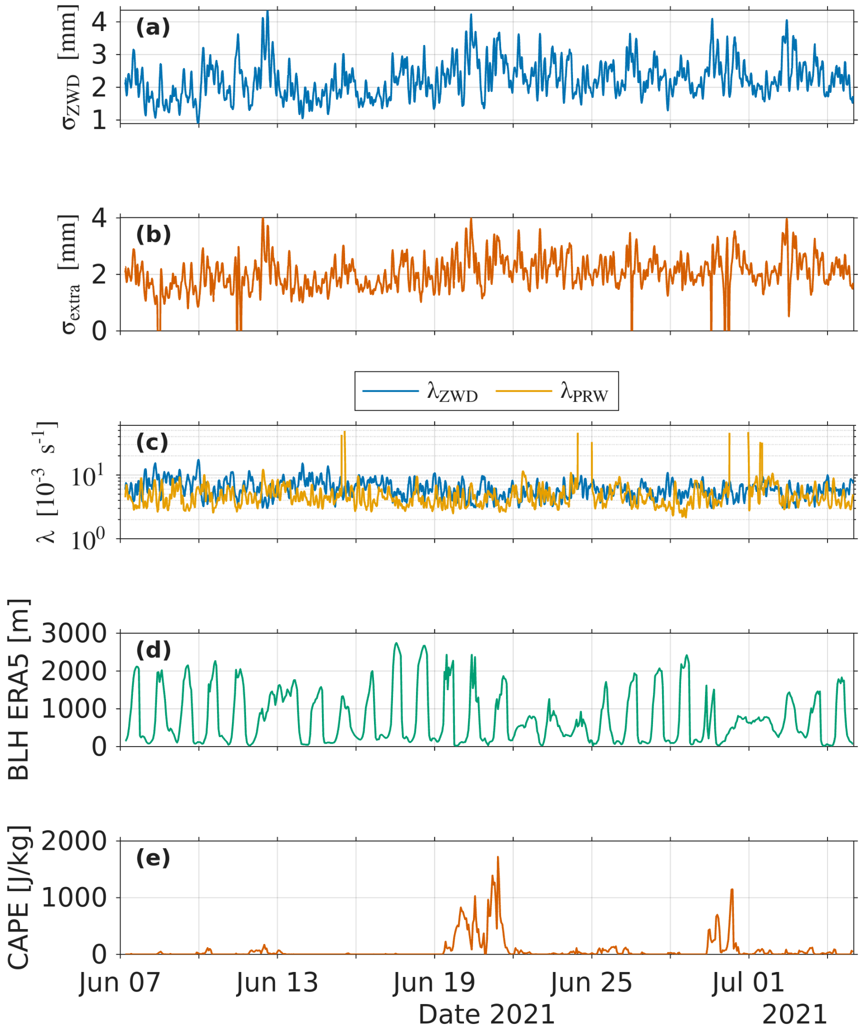

Figure 4. Time series overview of the 28-day intensive observation period (7 June to 4 July 2021) at Lindenberg. From top to bottom: GNSS-derived σ_{ZWD}, constructed σ_{extra}, λ_{ZWD} versus λ_{PRW}, ERA5 BLH, and ERA5 CAPE. All quantities are evaluated on 62.5 min sliding windows.

the thermodynamic BL depth and more to advection by the mean wind, consistent with Taylor's frozen turbulence hypothesis (Taylor, 1938). In this regime λ_{PRW} shifts from a BL geometric scaling towards an advective scaling. This is in line with wavenumber-frequency spectral models of the sheared convective BL, where the spectral peak is set by the balance between mean advection and random sweeping rather than by the BL depth alone (Ali et al., 2023).

https://doi.org/10.5194/egusphere-2026-4148
Preprint. Discussion started: 31 July 2026

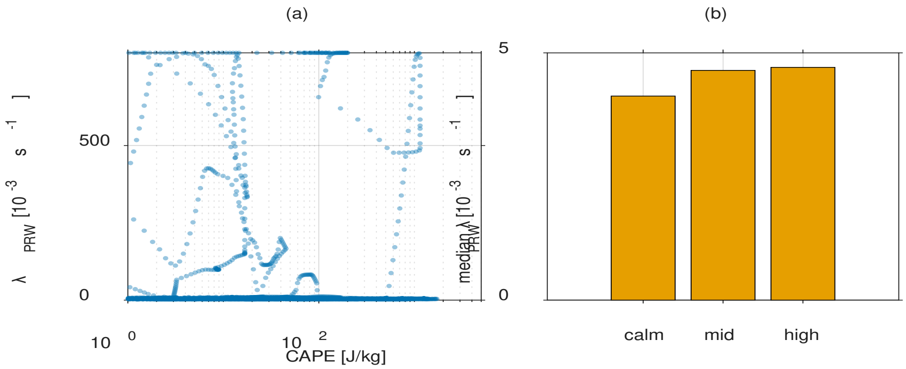

Figure 5. Regime shift of λ_{PRW} between calm and weakly unstable conditions. (a) Scatter plot of λ_{PRW} versus CAPE on a logarithmic scale. (b) Median λ_{PRW} stratified by CAPE tercile (calm, mid, high) showing the systematic shift. CAPE values remain weakly unstable throughout the summer 2021 window.

4.2 Geometric stability of λ_{ZWD}

The mirror result is that λ_{ZWD} shows no comparable shift across CAPE regimes. Computed against the continuous ERA5 BLH over all 8001 windows, the Spearman correlation $\rho(\lambda_{\text{ZWD}}, \text{BLH}_{\text{ERA5}})$ remains between -0.24 and -0.30 across all stratifications, a weak and stable association rather than a tracking relationship. The bootstrap delta on λ_{ZWD} between CAPE mid and high is -0.015 with CI95 $[-0.059, +0.029]$, which includes zero. The same stability is observed across all Falkenberg turbulence variables: delta ρ on u_* is only -0.026, more than an order of magnitude smaller than for λ_{PRW}. We return in Section 4.4 to the distinct question of how λ_{ZWD} relates to the radiosonde-derived BLH, which is the appropriate reference for a proxy assessment.

This contrast follows from the measurement geometry (Fig. 6). The GNSS PPP mapping function integrates obliquely along multiple satellite lines of sight, with elevation angles typically between 5 and 90 degrees (Wheelon, 2001; Kermarrec et al., 2020). The resulting ZWD reflects horizontal heterogeneities of water vapour in the slant cones crossing the BL top, which remain present and characteristically structured regardless of vertical stability. The MWR PRW, in contrast, integrates only along the vertical column, so its spectral signature directly reflects the vertical organisation, which changes with stratification.

4.3 Decomposition of σ_{extra}

The unexplained excess $\sigma_{\text{extra}} = \sqrt{\sigma^2_{\text{ZWD}} - \sigma^2_{\text{PRWeq}}}$ accounts for 93 percent of the GNSS variance. Its vertical origin can be located from the MWR humidity profile. Fitting $q(z)$ at 4 s cadence with the same Matérn procedure per altitude (43 levels), the correlation $\rho(\sigma_q(z), \sigma_{\text{extra}})$ peaks at $z = 2000$ m ($\rho = +0.22$), the typical summer BL top at Lindenberg. The variance maximum of σ_q sits lower, near 200 m, but does not correlate with σ_{extra}. Consistently, none of the Falkenberg in situ turbulence variables below 100 m correlate with σ_{extra} (all ρ below $+0.13$). The residual GNSS variance originates at the BL top rather than at the surface, as expected if it is a geometric signature of horizontal heterogeneity captured by the oblique rays.

https://doi.org/10.5194/egusphere-2026-4148
Preprint. Discussion started: 31 July 2026

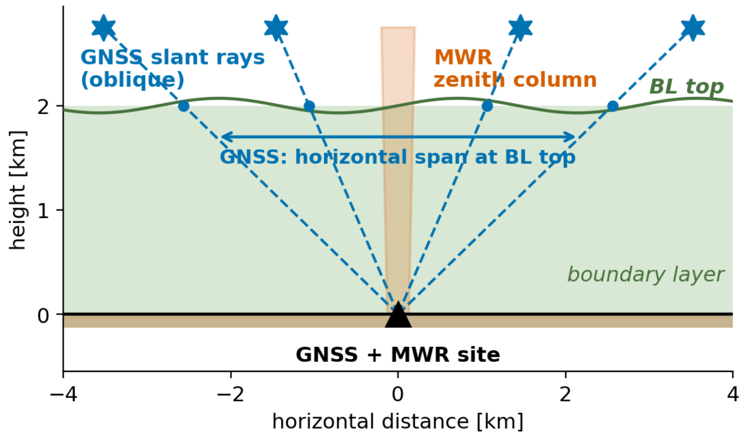

Figure 6. Measurement geometry. The MWR integrates along a single vertical column, while the GNSS integrates along multiple oblique slant rays that cross the BL top at horizontally separated points. The GNSS samples a horizontal span of the water vapour field at the BL top that the zenith MWR cannot resolve.

A processing-related fraction is also present, and we bound it rather than resolve it. Regressing σ_{extra} on the within-window scatter of the PPP correction series and on the inter-station differential $\mathrm{std}(\mathrm{ZWD}_{\mathrm{LDB2}} - \mathrm{ZWD}_{\mathrm{LIN0}})$ attributes of order a third of the excess to constellation geometry ($R^2 = 0.318$). This partition relies on the lower-quality LIN0 record and is indicative only; the remainder may mix antenna multipath with BL-top heterogeneity that the simple proxy does not capture. None of the observational case rests on it. The evidence that GNSS senses horizontal heterogeneity comes from the independent FOGHAT and MWR-triangle correlations of Section 4.5, which involve neither the correction series nor LIN0. A sidereal-day repeatability test finds no multipath signature: the autocorrelation of σ_{extra} at one sidereal day ($+0.09$) matches that at one solar day ($+0.09$), so the antenna environment does not carry the excess variance.

4.4 λ_{ZWD} as autonomous spectral observable

The third primary result emerges from treating λ_{ZWD} as a standalone observable. Since ZWD is derived from standard PPP at 30 s cadence on hundreds of IGS stations worldwide, the spectral fit produces λ_{ZWD} as a globally accessible quantity with no MWR or other infrastructure required. We characterise it here through its physical drivers, its stability relative to reanalysis, and its diurnal behaviour, and then clarify in the following paragraph what it does and does not measure with respect to BLH.

The diagnostic on the 28-day continuous time series identifies CAPE as the principal physical driver, $\rho(\lambda_{\mathrm{ZWD}}, \mathrm{CAPE}) = -0.32$, followed by BLH ERA5 ($-0.25$), TKE 90 m ($-0.24$), and u_* (-0.24). The correlation with wind speed alone is only -0.07, so λ_{ZWD} is not a disguised proxy of U.

Over the 28 days, λ_{ZWD} varies far less than the ERA5 BLH: its coefficient of variation is 0.32, against 0.90 for the ERA5 BLH. The two are different quantities, so this measures relative variability rather than a common scale, but the contrast is large: the horizontal coherence carried by λ_{ZWD} is about three times steadier over the period than the modelled BLH.

https://doi.org/10.5194/egusphere-2026-4148
Preprint. Discussion started: 31 July 2026

The diurnal contrast is pronounced (Fig. 7). The median λ_{ZWD} varies modestly through the day, from about 0.0052 s^{-1} at midday, when the BL is deep, to about 0.0071 s^{-1} at night, when it is shallow, a range of some 37 percent. Over the same hours the ERA5 BLH spans from about 130 m at night to about 1660 m at midday, a thirteenfold variation. The parameter λ_{ZWD} stays structured through the nocturnal stabilisation, when the thermodynamic BL collapses in ERA5. The signal may reflect residual organised structures, such as low-level jets or trapped gravity waves, that survive the formation of the stable BL, although the mechanism cannot be identified from this short record.

We also ask whether λ_{ZWD} knows anything about when the ERA5 BLH departs from the radiosondes. We measure that departure as $E = |\mathrm{BLH}_{\mathrm{ERA5}} - \mathrm{BLH}_{\mathrm{RS}}|$, the absolute difference between the ERA5 and radiosonde (Beyrich) BLHs. The two are weakly linked, $\rho(\lambda_{\mathrm{ZWD}}, E) = -0.18$, so λ_{ZWD} carries a small amount of information about the regimes where ERA5 and the radiosondes disagree, a disagreement already known to arise, in particular at night (Guo et al., 2021; Sinclair et al., 2022). This link is weak, rests on few soundings, and is not central to the conclusions.

4.4.1 λ_{ZWD} is not a BLH proxy

Whether λ_{ZWD} is simply a proxy for the BLH deserves a direct test. We assess it against the radiosonde BLH, which is a direct thermodynamic measurement rather than a model-derived field. The pooled correlation between λ_{ZWD} and the operationally-derived BLH from the Lindenberg radiosondes is weak and consistent across BLH methods: $\rho(\lambda_{\mathrm{ZWD}}, \mathrm{BLH}_{\mathrm{Beyrich}}) = -0.150$ with CI95 $[-0.349, +0.056]$ on 101 G-quality ascents using the operational Beyrich method (Beyrich and Leps, 2012), and $\rho(\lambda_{\mathrm{ZWD}}, \mathrm{BLH}_{\mathrm{parcel}}) = -0.154$ with CI95 $[-0.334, +0.039]$ on 113 ascents using a parcel method on the same radiosondes. The two methods agree on the pooled value despite producing BLH estimates that differ by a factor of four in median (1915 m for parcel, 463 m for Beyrich) and that correlate themselves differently with ERA5 ($\rho = +0.85$ for Beyrich and $+0.60$ for parcel). These radiosonde correlations are of the same weak magnitude as the continuous ERA5 association reported in Section 4.2. The relationship is weak and not an artefact of a particular reference. The intervals are wide on this sounding count and do not by themselves exclude a modest association; the interpretation rests on their consistency across methods, together with the strong, opposite-signed heterogeneity correlations of Section 4.5, rather than on this test alone. For comparison, the same test for the MWR observable returns $\rho(\lambda_{\mathrm{PRW}}, \mathrm{BLH}_{\mathrm{Beyrich}}) = -0.335$, as expected for a vertical-only quantity that tracks a vertical BLH measure.

This pattern is the expected one. If λ_{ZWD} were a BLH proxy, the correlation should approach that between two independent BLH estimates, of order $+0.85$. The fact that λ_{ZWD} correlates only weakly and modestly with BLH, while showing strong, monotone correlations with direct measurements of horizontal heterogeneity (Section 4.5), supports the interpretation that λ_{ZWD} reflects a horizontal coherence sensed at the BL top through the oblique GNSS multi-ray integration, distinct from the thermodynamic BLH. The complementary observable σ_{ZWD} shows a pooled correlation $\rho(\sigma_{\mathrm{ZWD}}, \mathrm{BLH}_{\mathrm{Beyrich}}) = +0.202$ with CI95 $[+0.005, +0.395]$ excluding zero, consistent with the orthogonal information carried by the pair $(\lambda_{\mathrm{ZWD}}, \sigma_{\mathrm{ZWD}})$.

https://doi.org/10.5194/egusphere-2026-4148
Preprint. Discussion started: 31 July 2026

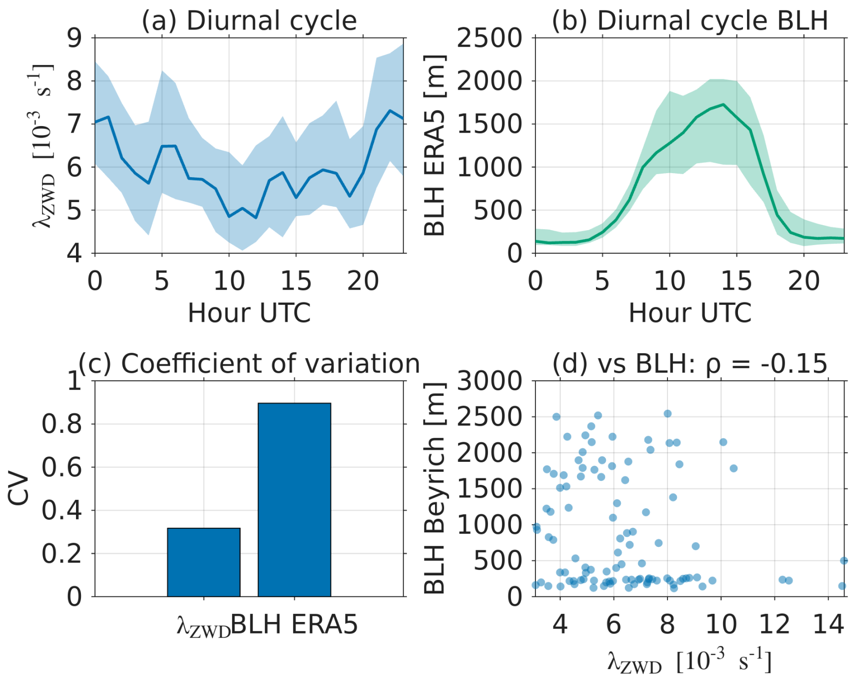

Figure 7. λ_{ZWD} as an autonomous spectral observable. (a) Diurnal cycle of λ_{ZWD} with interquartile range. (b) Diurnal cycle of ERA5 BLH for comparison; the nocturnal collapse is absent from λ_{ZWD}. (c) Coefficient of variation comparison demonstrating the higher stability of λ_{ZWD}. (d) Scatter plot of λ_{ZWD} versus the operational BLH from radiosondes (Beyrich method, 101 G-quality soundings).

4.5 Direct observational validation of the horizontal heterogeneity signature

The interpretation that σ_{extra} and λ_{ZWD} reflect horizontal heterogeneity at the BL top, captured geometrically by the multi-ray oblique integration of GNSS, can be tested directly against the FOGHAT azimuth-scanning HATPRO and the regional-scale scintillometer (Section 2.7).

4.5.1 FOGHAT azimuthal heterogeneity index

For each 62.5 min window aligned with t_{grid}, we bin the continuous FOGHAT scan into 36 azimuth sectors and compute the azimuthal heterogeneity σ_{azi} as the standard deviation of the off-zenith PRW values across them, after subtracting a 15 min moving mean to filter slow temporal variations. The samples are grouped into 8 azimuthal bins of 45° width to isolate the spatial component. The resulting σ_{azi} represents a direct, radiometric measurement of horizontal water vapour heterogeneity above the Lindenberg site at the BL top, fully independent of the GNSS observable (Fig. 8).

These cross-correlations are collected in Table 1.

The GNSS-derived observables correlate clearly and monotonically with the FOGHAT azimuthal heterogeneity (positive for σ_{ZWD} and σ_{extra}, negative for λ_{ZWD} as expected for an inverse coherence scale, since a more coherent field corresponds to a

https://doi.org/10.5194/egusphere-2026-4148
Preprint. Discussion started: 31 July 2026

Table 1. Spearman rank correlations ρ between the GNSS and MWR spectral observables and the independent measures. Horizontal heterogeneity is given by the FOGHAT azimuthal spread σ_{azi} (hectometre to kilometre scale) and the MWR triangle inter-site spread σ_{inter} (5–6 km). The surface null test correlates σ_{extra} with the path-integrated scintillometer fluxes and structure parameter and with the Falkenberg point-sensor flux. The tabulated σ_{inter} is the Lindenberg–Birkholz pair; the instantaneous spread across the three sites correlates with σ_{extra} at $+0.367$.

	Measure	σ_{ZWD}	σ_{extra}	λ_{ZWD}	λ_{PRW}
Horizontal	FOGHAT σ_{azi} (hectom–km)	$+0.433$	$+0.294$	-0.375	-0.061
heterogeneity	Triangle σ_{inter} (5–6 km)	$+0.525$	$+0.278$	-0.438	-0.079
Surface	$\|H\|$ scint. (4.85 km, 43 m)		$+0.033$		
turbulence	$\|LE\|$ scint. (4.85 km)		$+0.082$		
(null test)	$\log_{10} C_n^2$(MW)		-0.055		
	$\|H\|$ Falkenberg (2.3 m)		$+0.048$		

smaller λ_{ZWD}). In contrast, the MWR vertical-only λ_{PRW} shows no correlation, with $\rho = -0.061$ falling within the bootstrap noise level. Stratification by tercile of σ_{azi} shows a monotone progression of σ_{extra} from 1.84 mm (low heterogeneity) to 2.21 mm (high heterogeneity).

This contrast supports the geometric interpretation. The GNSS ZWD obtained from standard PPP appears to capture horizontal atmospheric structure that vertical MWR profiling does not resolve, and the magnitude of the captured signal increases with an independently measured azimuthal variance of the water vapour field.

FOGHAT itself scans at 30° elevation, so σ_{azi} is an obliquely integrated quantity, like the GNSS ZWD. Their correlation could arise simply because both instruments look sideways, rather than because they sense the same water vapour field. The MWR triangle of the next subsection settles this point. Its inter-site spread comes from zenith-pointing PRW records that share no viewing geometry with the GNSS, yet it correlates with σ_{ZWD} just as σ_{azi} does. A shared oblique-viewing artefact cannot produce a correlation with zenith instruments, so the signal must reflect a real horizontal field. A second, weaker check points the same way: within the same HATPRO family, the purely vertical λ_{PRW} shows no correlation with σ_{azi} at all, so the association is not a generic feature of radiometer data.

4.5.2 Regional-scale scintillometer fluxes and structure parameters

To exclude that σ_{extra} has a surface-dynamical origin, we correlate it with three independent surface-layer turbulence proxies measured on the 4.85 km Falkenberg-Lindenberg path at 43 m effective height (Section 2.7): the regional-scale sensible heat flux $|H|_{\text{scint}}$, the latent heat flux $|LE|_{\text{scint}}$, and the microwave refractive index structure parameter C_n^2(MW) reconstructed from the OMS structure parameters (Section 3.3). We add the Falkenberg point-sensor flux at 2.3 m as a fourth, near-ground proxy.

https://doi.org/10.5194/egusphere-2026-4148
Preprint. Discussion started: 31 July 2026

The four correlations are all near zero (Table 1, bottom rows). The point-sensor flux at 2.3 m, the regional-scale fluxes integrated over 4.85 km at 43 m, and the path-integrated C_n^2(MW) at the same height all return $|\rho| < 0.10$. The latter is the most physically direct test, since C_n^2(MW) at 11 GHz is dominated by water vapour fluctuations, the same quantity that drives σ_{extra} through the ZWD. The null result at 43 m demonstrates that the heterogeneity sensed by GNSS does not originate in the surface layer, even when integrated over 4.85 km horizontally.

Combined with the positive boundary-layer-top signature at $z = 2000$ m from MWR humidity profiles (Section 4.3) and the positive horizontal heterogeneity correlations at scales of hectometres to kilometres (FOGHAT azimuthal, MWR triangle), this null result defines a clear vertical signature. σ_{extra} has no measurable signal below approximately 100 m and a strong signal at the BL top, exactly as expected from the geometric integration of GNSS slant rays.

4.5.3 Multi-site MWR coherence at the 5–6 km supersites scale

A third independent test of the horizontal heterogeneity signature exploits the FESSTVaL triangle of three HATPRO MWRs providing zenith PRW: RAOHAT at Lindenberg (LDB), HAMHAT at Birkholz (BHK), and SUNHAT at Falkenberg (FBG) (Section 2.7). The three PRW time series are aligned on a common 1 min grid through linear interpolation, then the inter-site differential standard deviation is computed on the same 62.5 min windows as the spectral parameters:

$$\sigma_{\text{inter}}(t) = \text{std}_w(\text{PRW}_{\text{LDB}} - \text{PRW}_{\text{BHK}}), \tag{5}$$

plus the analogous quantities for the Lindenberg-Falkenberg (4.85 km) and Birkholz-Falkenberg (6 km) pairs, and the instantaneous spread of PRW across the three sites.

The cross-correlations with the GNSS spectral parameters confirm the pattern already observed at the azimuthal scale (Table 1).

The GNSS observables again show monotone correlations with the inter-site MWR differential, while the MWR vertical-only λ_{PRW} remains in the bootstrap noise level. Across the three supersites, the inter-site spread of PRW (the instantaneous standard deviation across sites, median 0.53 kg m^{-2}) correlates with σ_{extra} at $\rho = +0.367$ and increases by 39 percent from the lowest to the highest CAPE tercile (0.45 to 0.62 kg m^{-2}). This growth of inter-site heterogeneity under weakly unstable conditions matches the regime shift of Section 4.1. Taken pairwise, the Spearman correlations with σ_{extra} are $+0.278$, $+0.248$ and $+0.283$ for Lindenberg–Birkholz, Lindenberg–Falkenberg and Birkholz–Falkenberg (median pair spreads 0.29, 0.28 and 0.32 kg m^{-2}); Table 1 reports the Lindenberg–Birkholz pair.

4.5.4 Robustness to common drivers, significance and stationarity

The GNSS correlations are not an artefact of a shared moisture or activity driver. Controlling jointly for TCWV, the diurnal cycle, CAPE, the 10 m wind and the ERA5 BLH by partial Spearman correlation, $\rho(\sigma_{\text{ZWD}}, \sigma_{\text{azi}})$ falls from $+0.433$ to $+0.289$ and $\rho(\sigma_{\text{ZWD}}, \sigma_{\text{inter}})$ from $+0.525$ to $+0.356$, each keeping its sign, and λ_{ZWD} likewise stays negative (-0.24 and -0.28). The strongest single candidate confounder, column water vapour, barely affects them: controlling for TCWV alone leaves $+0.387$ and $+0.488$. Block-bootstrap 95 % confidence intervals that respect the window overlap exclude zero for every GNSS ob-

https://doi.org/10.5194/egusphere-2026-4148
Preprint. Discussion started: 31 July 2026

servable (σ_{ZWD} versus σ_{azi}, $[+0.36,+0.50]$; versus σ_{inter}, $[+0.45,+0.59]$; λ_{ZWD}, $[-0.45,-0.30]$ and $[-0.51,-0.36]$; circular-shift $p<0.001$ throughout), whereas the corresponding λ_{PRW} intervals include zero ($[-0.15,+0.02]$ and $[-0.19,+0.03]$). The associations are stationary over the four weeks: recomputed on quarter-period sub-samples, $\rho(\sigma_{\mathrm{ZWD}},\sigma_{\mathrm{azi}})$ stays within $[+0.33,+0.43]$ and $\rho(\sigma_{\mathrm{ZWD}},\sigma_{\mathrm{inter}})$ within $[+0.42,+0.62]$.

The observational tests address two distinct axes. Two of them probe horizontal heterogeneity at different scales (FOGHAT azimuthal scanning at the hectometre to kilometre scale, and the MWR triangle at the 5–6 km supersites zenith scale) and both show a positive association with σ_{ZWD}. The third (the optical-microwave scintillometer integrated over the 4.85 km surface-layer path) is a vertical control on the origin of the signal and returns a near-zero correlation. This argues against a surface-dynamical source. Taken together they fit an interpretation in which GNSS-derived spectral observables are associated with horizontal water vapour heterogeneity at the BL top, with a magnitude that increases with the heterogeneity independently measured by collocated radiometric instruments. The MWR vertical-only λ_{PRW} shows no comparable association, with correlations within the bootstrap noise level at both horizontal scales. This follows from the geometric difference between oblique GNSS multi-ray integration and zenith MWR profiling.

5 Discussion

We now interpret the four results and their supporting tests through the measurement geometry that distinguishes the oblique GNSS integration from the vertical MWR column, then set out how the autonomous observable could be used.

5.1 Interpretation

GNSS ZWD and MWR PRW provide complementary observations of the same atmospheric column, each carrying information the other does not. The MWR sees the vertical integral directly, with high cadence and good radiometric accuracy. The GNSS sees an oblique multi-ray integral. Its geometric content captures the horizontal heterogeneity invisible to the vertical MWR. The two observables differ by a factor of 3.7 in standard deviation.

λ_{ZWD} stays stable across regimes, and in particular it is not a disguised wind proxy ($\rho(\lambda_{\mathrm{ZWD}},U)=-0.07$), whereas the single-column λ_{PRW} inherits the advective Taylor scaling once the flow becomes weakly unstable. This stability follows from the multi-ray averaging behind the ZWD. At each epoch the ZWD combines the slant delays to all visible satellites, whose piercing points at the BL top spread over a horizontal disk, a few kilometres across at high elevation and some twenty kilometres near the horizon; the horizontal offset of a ray at height z and elevation ε is $d=z/\tan\varepsilon$. This is ≈ 3.5 km at $\varepsilon=30°$ and ≈ 11 km at $\varepsilon=10°$ for $z=2000$ m. The average pools many azimuths and elevations, and the piercing points move as the satellites track across the sky, so the observable does not follow the vapour field along the single advecting direction that a fixed zenith column sees. λ_{ZWD} also persists through the nocturnal stabilisation, when the horizontal coherence of water vapour at the BL top, set by the sub-mesoscale organisation of the moisture field, does not collapse with the thermodynamic BL depth. A full account of how this moving multi-ray geometry sets λ_{ZWD} needs forward-modelling of the ZWD from a resolved vapour field along the true slant geometry, which we set out in Section 5.2. The same disk radius spans both scales at which the signature is

https://doi.org/10.5194/egusphere-2026-4148
Preprint. Discussion started: 31 July 2026

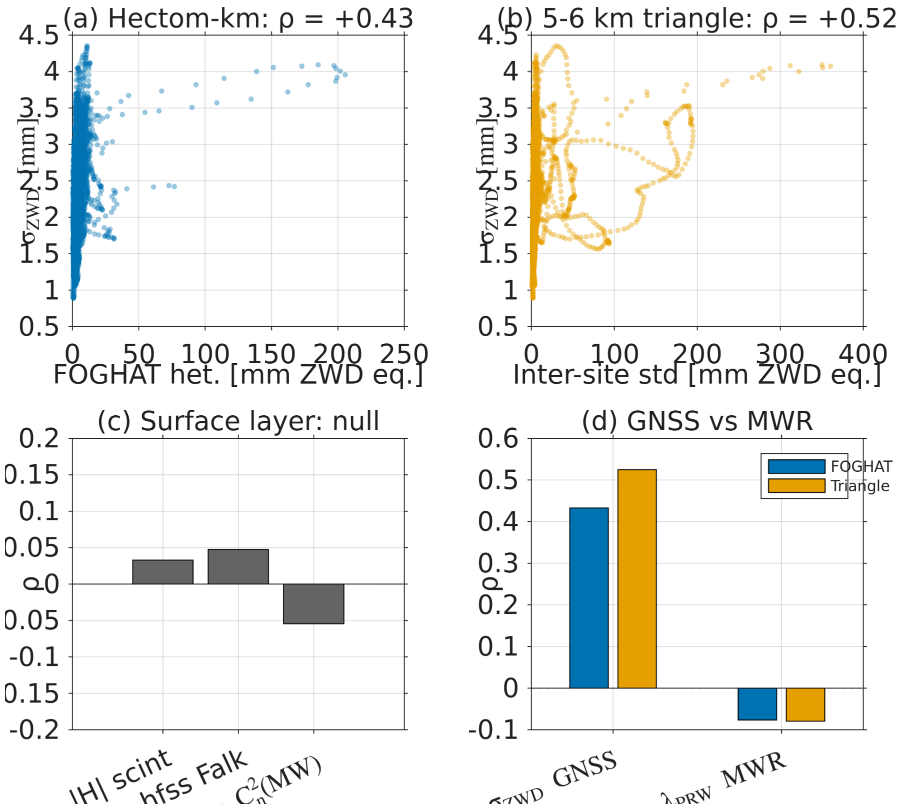

Figure 8. Observational support at two horizontal scales together with a surface null test. (a) σ_{ZWD} versus the FOGHAT azimuthal heterogeneity at the hectometre to kilometre scale ($\rho = +0.433$). (b) σ_{ZWD} versus the MWR triangle inter-site standard deviation at the 5–6 km supersites scale ($\rho = +0.525$). (c) Near-zero correlation of σ_{extra} with surface-layer turbulence proxies, used as a control on the origin of the signal. (d) Contrast between GNSS σ_{ZWD} and MWR vertical λ_{PRW} across the two horizontal scales.

confirmed, the hectometre-to-kilometre FOGHAT footprint and the 5–6 km supersites triangle, so a single geometric argument predicts a response at both.

The spectral scale λ then carries a different meaning depending on the integrator. For the vertical column (PRW), λ_{PRW} reflects the dominant vertical structure of the column. That structure scales with BL depth in calm regimes and moves towards an advective scaling as the flow becomes weakly unstable. For the oblique multi-ray observable (ZWD), λ_{ZWD} reflects horizontal coherence at the layer of strongest gradient, the BL top, and stays structured across all regimes. The MWR triangle is what turns this interpretation from an inference into a measurement. Because the three zenith radiometers sample the same vapour field 5–6 km apart with no shared oblique geometry, their inter-site spread is an external, geometry-independent measure of horizontal heterogeneity. Its correlation with σ_{ZWD} (Table 1) then fixes what the GNSS spectral amplitude responds to.

The horizontal coherence length implied by λ_{ZWD} places the signal in the sub-mesoscale range of water vapour organisation, between the turbulent scale and the mesoscale, where moisture is neither well mixed nor smoothly varying. FESSTVaL was

https://doi.org/10.5194/egusphere-2026-4148
Preprint. Discussion started: 31 July 2026

designed precisely to resolve these scales. Its dense surface network at Lindenberg documented cold pools and gust fronts with horizontal extents of hundreds of metres to a few kilometres (Kirsch et al., 2022a), the same range as the disk that the GNSS slant rays sample at the BL top. Their dynamical importance is well established. Small-scale water vapour heterogeneity exerts a first-order control on where and when moist convection is initiated (Weckwerth, 2000; Hohenegger et al., 2023). Observing lower-tropospheric humidity at these scales has long been a recognised gap in the observing system (Wulfmeyer et al., 2015). The GNSS spectral scale adds a quantity that is continuous in time and available at any existing station. It complements the campaign and snapshot instruments that have carried most of the sub-mesoscale moisture record so far.

Once treated as autonomous quantities accessible from any standard GNSS solution, the observables $(\lambda_{\mathrm{ZWD}}, \sigma_{\mathrm{ZWD}})$ provide a diagnostic that complements existing reanalysis products. Their content is largely orthogonal to the thermodynamic BL depth: λ_{ZWD} correlates only weakly with radiosonde and reanalysis BLH, yet it stays structured through the nocturnal collapse of the modelled layer. It is also three times more stable than the ERA5 BLH. The GNSS pair reports on the horizontal organisation of water vapour at the BL top. Neither a vertical sounding nor a reanalysis BL scheme resolves that organisation directly.

These conclusions come with limits. The signal is modest on a 28-day single-site window, and the supporting correlations are moderate (R^2 of about 0.18 and 0.28 at the two horizontal scales). Their size reflects the sampling geometry as much as the strength of the effect. The GNSS observable averages slant rays over all azimuths and a wide range of elevations, whereas FOGHAT scans a single elevation and the triangle samples only three fixed points. The spatial supports of the compared quantities overlap without coinciding. Even when the underlying field is shared, that mismatch dilutes the rank correlation. A moderate but consistent correlation across independent instruments and scales is the expected signature of a real common field sampled through different apertures. A second limit concerns the decomposition of σ_{extra}. About a third is associated with constellation geometry rather than atmosphere, on the basis of the lower-quality LIN0 differential, so the partition is indicative only. It bounds the processing-related contribution without carrying the physical claim. That claim rests entirely on the external FOGHAT and triangle correlations, which involve neither LIN0 nor the correction series. Finally, the reading of σ_{extra} as a BL-top signature rests on the vertical structure of the correlations, positive at the BL top and null at the surface, rather than on a height-resolved measurement of the GNSS contribution itself. These limits set the agenda below.

5.2 Outlook

The practical value of the result follows from where λ_{ZWD} comes from. It is produced by the same PPP that thousands of IGS and national reference stations run continuously, at no additional instrumental cost and independent of cloud, daylight or the diurnal cycle. Three uses follow. As a stable, night-persistent measure of horizontal coherence at the BL top, λ_{ZWD} can serve as an independent check on reanalysis BL schemes, which are known to decouple from observations at night; a systematic comparison of λ_{ZWD} against the reanalysis error $E = |\mathrm{BLH}_{\mathrm{ERA5}} - \mathrm{BLH}_{\mathrm{RS}}|$ across many stations would test whether the weak link found here ($\rho = -0.18$) strengthens into a usable flag. As a candidate diagnostic for the pre-convective organisation of the moisture field, the pair $(\lambda_{\mathrm{ZWD}}, \sigma_{\mathrm{ZWD}})$ tracks the growing horizontal heterogeneity in the hours when the field organises, where σ_{ZWD} increases with heterogeneity, and its predictive value could be tested directly against convective initiation from radar. That would close the loop back to the moisture-control question behind the campaign (Weckwerth, 2000; Hohenegger

https://doi.org/10.5194/egusphere-2026-4148
Preprint. Discussion started: 31 July 2026

et al., 2023). Finally, because the observable is available on dense networks, maps of λ_{ZWD} and σ_{ZWD} could resolve the spatial pattern of this coherence rather than a single-station value. Such maps could then be assimilated alongside the ZWD already ingested operationally in numerical weather prediction (Guerova et al., 2016).

Turning these possibilities into quantitative tools requires three steps that the present dataset motivates but cannot complete. First, the statistics should be rebuilt on the full multi-year LDB2 and RAOHAT archive, about 210000 spectral-fit windows, for season-resolved confidence intervals in place of the 28-day estimates here; if the moderate correlations of Table 1 are the diluted image of a real field, they should sharpen and stabilise with season and sample size rather than regress towards zero. Second, the autonomous observable should be evaluated at stations that pair a continuous GNSS record with operational radiosondes and, ideally, an MWR, such as Payerne (Löhnert and Maier, 2012), so that the pair $(\lambda_{\mathrm{ZWD}}, \sigma_{\mathrm{ZWD}})$ can be regressed jointly against BLH and against reanalysis error to quantify its independent information content; a finding that λ_{ZWD} tracks horizontal heterogeneity but not the BLH at sites of differing climate would generalise the Lindenberg result, whereas a strong BLH correlation elsewhere would bound its interpretation. Third, large eddy simulations of a FESSTVaL convective case, such as 14 June 2021, with ZWD and PRW computed directly from the model vapour field along the true slant and zenith geometries, would close the geometric argument by reproducing the observed contrast from first principles, and would count against it if the modelled λ_{ZWD} tracked the modelled BL depth. Cross-validation against satellite TCWV, for instance from Sentinel-3 OLCI at a few hundred metres resolution, would add a horizontal snapshot at a scale between the FOGHAT and triangle tests.

6 Conclusions

Four results are established on the 28-day FESSTVaL window at Lindenberg. The spectral parameter λ_{PRW} undergoes a regime shift between calm and weakly unstable conditions, from a BL geometric signature towards an advective one, supported independently by in situ tower turbulence. The spectral parameter λ_{ZWD} stays stable across all regimes. Because the GNSS mapping function averages over many oblique rays, it is insensitive to the vertical changes that shift λ_{PRW} and instead reflects the horizontal coherence at the BL top. The unexplained GNSS variance σ_{extra} is partly associated with constellation geometry (about 32 percent), and the remainder originates principally from the BL top near $z = 2000$ m rather than from surface turbulence. The geometric interpretation is supported observationally at two horizontal scales together with a vertical surface null test. At the hectometre to kilometre scale, the FOGHAT azimuth-scanning HATPRO yields $\rho(\sigma_{\mathrm{ZWD}}, \sigma_{\mathrm{azi}}) = +0.433$ while $\rho(\lambda_{\mathrm{PRW}}, \sigma_{\mathrm{azi}}) = -0.061$. At the 5–6 km supersites scale, the MWR triangle of zenith HATPROs at Lindenberg, Birkholz, and Falkenberg yields $\rho(\sigma_{\mathrm{ZWD}}, \sigma_{\mathrm{inter}}) = +0.525$ while $\rho(\lambda_{\mathrm{PRW}}, \sigma_{\mathrm{inter}}) = -0.079$. The regional-scale scintillometer over 4.85 km at 43 m effective height and the Falkenberg point-sensor fluxes at 2.3 m both show near-zero correlation with σ_{extra} ($\rho \approx 0.03$ and 0.05 respectively), which argues against a surface-dynamical origin. Together these tests indicate that GNSS-derived spectral observables capture horizontal atmospheric structure that vertical MWR sounding does not resolve, with a magnitude that increases with the independently measured heterogeneity at the corresponding spatial scale. We emphasise that the supporting correlations are moderate (R^2 of about 0.18 and 0.28 at the two horizontal scales); their value lies in the consistent sign

https://doi.org/10.5194/egusphere-2026-4148
Preprint. Discussion started: 31 July 2026

and monotone behaviour across independent instruments and scales, together with the contrasting near-zero response of the vertical-only λ_{PRW}, rather than in their individual magnitude.

A fifth result, more exploratory, is that λ_{ZWD} treated as an autonomous spectral observable captures a horizontal coherence at Lindenberg that is more stable than ERA5 BLH (CV 0.32 vs 0.90) and persists through the nocturnal cycle when the thermodynamic BLH collapses in reanalysis. The pooled correlation with radiosonde BLH is weak and consistent across BLH methods ($\rho \approx -0.15$ with both Beyrich and parcel methods), which is the pattern expected for a horizontal coherence sensed at the BL top through oblique multi-ray integration rather than for a BLH proxy.

The directions needed to consolidate and exploit these results, from a multi-year reprocessing of the LDB2 and RAOHAT records to a large eddy simulation closure of the geometric argument, are set out in the Outlook (Section 5.2).

Data availability. FESSTVaL observations are available through the ICDC repository of Universität Hamburg, https://www.cen.uni-hamburg.de/en/icdc/research/samd/observational-data/short-term-observations/fesstval.html. The MWR observations (RAOHAT, FOGHAT, HAMHAT, SUNHAT) are published by Löhnert, Knist, Böck and Pospichal (2022, DOI 10.25592/uhhfdm.10198). The Falkenberg turbulence dataset is published by Frank Beyrich (DWD MOL-RAO) on the FDR Hamburg repository (Beyrich, 2024, DOI 10.25592/uhhfdm.14239). The operational radiosonde BLHs (Beyrich method), the BLS-900 optical C_n^2 time series, and the OMS structure parameters (C_T^2, C_q^2, C_{Tq}) were provided by DWD MOL-RAO (F. Beyrich, personal communication, 2026) and are available from DWD on request. The raw radiosonde profiles used for the parcel BLH are available from the FESSTVaL radiosonde dataset (Kirsch et al., 2022b). The published scintillometer level-2 fluxes are available at DOI 10.25592/uhhfdm.11980 (Päschke et al., 2023). The IGS station LDB2 is operated by the Federal Agency for Cartography and Geodesy (BKG) and data is available through the IGS network. ERA5 reanalysis data is provided by the Copernicus Climate Change Service (C3S). The processed ZWD, PRW and auxiliary time series used in this study, together with the scripts that generate the figures, are archived at https://doi.org/10.25835/g8w2ezl4 (Kermarrec, 2026).

Author contributions. GK designed the study, performed the spectral analysis and the validation against the auxiliary observations, and wrote the manuscript. ZD contributed GNSS processing expertise and advised on the PPP setup. XC contributed to the interpretation of the radiometric and water vapour diagnostics. NP carried out part of the analysis and revised the manuscript. All authors discussed the results and commented on the manuscript.

Competing interests. The authors declare no competing interests.

Acknowledgements. PRIDE PPP-AR software developed by the GNSS Research Center, Wuhan University. We thank Frank Beyrich (DWD MOL-RAO) for providing the radiosonde, scintillometer and tower turbulence data and for valuable discussions on boundary-layer observations.

https://doi.org/10.5194/egusphere-2026-4148
Preprint. Discussion started: 31 July 2026

References

Ali, N., Mellado, J. P., and Wilczek, M.: A wavenumber–frequency spectrum model for sheared convective atmospheric boundary layer flows, Journal of the Atmospheric Sciences, 80, 763–776, https://doi.org/10.1175/JAS-D-22-0079.1, 2023.

Bender, M., Dick, G., Ge, M., Deng, Z., Wickert, J., Kahle, H.-G., Raabe, A., and Tetzlaff, G.: Development of a GNSS water vapour tomography system using algebraic reconstruction techniques, Advances in Space Research, 47, 1704–1720, https://doi.org/10.1016/j.asr.2010.05.034, 2011.

Bevis, M., Businger, S., Herring, T. A., Rocken, C., Anthes, R. A., and Ware, R. H.: GPS meteorology: Remote sensing of atmospheric water vapor using the global positioning system, Journal of Geophysical Research: Atmospheres, 97, 15 787–15 801, https://doi.org/10.1029/92JD01517, 1992.

Bevis, M., Businger, S., Chiswell, S., Herring, T. A., Anthes, R. A., Rocken, C., and Ware, R. H.: GPS meteorology: Mapping zenith wet delays onto precipitable water, Journal of Applied Meteorology, 33, 379–386, https://doi.org/10.1175/1520-0450(1994)033<0379:GMMZWD>2.0.CO;2, 1994.

Beyrich, F.: Falkenberg basic and turbulence measurements during FESSTVaL 2021, Dataset, https://doi.org/10.25592/uhhfdm.14239, 2024.

Beyrich, F. and Adam, W. K.: Site and Data Report for the Lindenberg Reference Site in CEOP – Phase I, Tech. Rep. 230, Deutscher Wetterdienst, 2007.

Beyrich, F. and Leps, J.-P.: An operational mixing height data set from routine radiosoundings at Lindenberg: methodology, Meteorologische Zeitschrift, 21, 337–348, https://doi.org/10.1127/0941-2948/2012/0333, 2012.

Böck, T., Löffler, M., Marke, T., Pospichal, B., Knist, C., and Löhnert, U.: Instrument uncertainties of network-suitable ground-based microwave radiometers: overview, quantification, and mitigation strategies, Atmospheric Measurement Techniques, 18, 6251–6275, https://doi.org/10.5194/amt-18-6251-2025, 2025.

Champollion, C., Masson, F., Bouin, M.-N., Walpersdorf, A., Doerflinger, E., Bock, O., and Van Baelen, J.: GPS water vapour tomography: preliminary results from the ESCOMPTE field experiment, Atmospheric Research, 74, 253–274, https://doi.org/10.1016/j.atmosres.2004.04.003, 2005.

Chen, G. and Herring, T. A.: Effects of atmospheric azimuthal asymmetry on the analysis of space geodetic data, Journal of Geophysical Research: Solid Earth, 102, 20 489–20 502, https://doi.org/10.1029/97JB01739, 1997.

Crewell, S. and Löhnert, U.: Accuracy of boundary layer temperature profiles retrieved with multifrequency, multiangle microwave radiometry, IEEE Transactions on Geoscience and Remote Sensing, 45, 2195–2201, https://doi.org/10.1109/TGRS.2006.888434, 2007.

Flores, A., Ruffini, G., and Rius, A.: 4D tropospheric tomography using GPS slant wet delays, Annales Geophysicae, 18, 223–234, https://doi.org/10.1007/s00585-000-0223-7, 2000.

Geng, J., Chen, X., Pan, Y., Mao, S., Li, C., Zhou, J., and Zhang, K.: PRIDE PPP-AR: an open-source software for GPS PPP ambiguity resolution, GPS Solutions, 23, 1–10, https://doi.org/10.1007/s10291-019-0888-1, 2019.

Guerova, G., Jones, J., Douša, J., Dick, G., de Haan, S., Pottiaux, E., Bock, O., Pacione, R., Elgered, G., Vedel, H., and Bender, M.: Review of the state of the art and future prospects of the ground-based GNSS meteorology in Europe, Atmospheric Measurement Techniques, 9, 5385–5406, https://doi.org/10.5194/amt-9-5385-2016, 2016.

Guillaumin, A. P., Sykulski, A. M., Olhede, S. C., and Simons, F. J.: The debiased spatial Whittle likelihood, Journal of the Royal Statistical Society Series B: Statistical Methodology, 84, 1526–1557, https://doi.org/10.1111/rssb.12539, 2022.

https://doi.org/10.5194/egusphere-2026-4148
Preprint. Discussion started: 31 July 2026

Guo, J., Zhang, J., Yang, K., Liao, H., Zhang, S., Huang, K., Lv, Y., Shao, J., Yu, T., Tong, B., et al.: Investigation of near-global daytime boundary layer height using high-resolution radiosondes: first results and comparison with ERA5, MERRA-2, JRA-55, and NCEP-2 reanalyses, Atmospheric Chemistry and Physics, 21, 17 079–17 097, https://doi.org/10.5194/acp-21-17079-2021, 2021.

Hersbach, H., Bell, B., Berrisford, P., Hirahara, S., Horányi, A., Muñoz-Sabater, J., Nicolas, J., Peubey, C., Radu, R., Schepers, D., Simmons, A., Soci, C., Abdalla, S., Abellan, X., Balsamo, G., Bechtold, P., Biavati, G., Bidlot, J., Bonavita, M., et al.: The ERA5 global reanalysis, Quarterly Journal of the Royal Meteorological Society, 146, 1999–2049, https://doi.org/10.1002/qj.3803, 2020.

Hill, R. J.: Algorithms for obtaining atmospheric surface-layer fluxes from scintillation measurements, Journal of Atmospheric and Oceanic Technology, 14, 456–467, https://doi.org/10.1175/1520-0426(1997)014<0456:AFOASL>2.0.CO;2, 1997.

Hohenegger, C., Ament, F., Beyrich, F., Löhnert, U., Rust, H., et al.: FESSTVaL: The Field Experiment on Submesoscale Spatio-Temporal Variability in Lindenberg, Bulletin of the American Meteorological Society, 104, E1875–E1892, https://doi.org/10.1175/BAMS-D-21-0330.1, 2023.

Kermarrec, G.: On a correlation model for laser scanners: a large eddy simulation experiment, Remote Sensing, 16, 3545, https://doi.org/10.3390/rs16193545, 2024.

Kermarrec, G.: Processed GNSS ZWD, MWR PRW and auxiliary spectral time series for FESSTVaL Lindenberg 2021, with figure-generating scripts, https://doi.org/10.25835/g8w2ezl4, dataset, 2026.

Kermarrec, G. and Schön, S.: On the Matérn covariance family: a proposal for modeling temporal correlations based on turbulence theory, Journal of Geodesy, 88, 1061–1079, https://doi.org/10.1007/s00190-014-0743-7, 2014.

Kermarrec, G., Loße, E., and Schoen, S.: On the determination of the atmospheric outer scale length of turbulence using GPS phase difference observations: the Seewinkel network, Earth, Planets and Space, 72, 184, https://doi.org/10.1186/s40623-020-01308-w, 2020.

Kermarrec, G., Calbet, X., Deng, Z., and Carbajal Henken, C.: Measurement report: Can zenith wet delay from GNSS “see” atmospheric turbulence? Insights from case studies across diverse climate zones, Atmospheric Chemistry and Physics, 25, 3567–3590, https://doi.org/10.5194/acp-25-3567-2025, 2025.

Kermarrec, G., Schrader, T., Calbet, X., and Deng, Z.: GNSS zenith wet delay as a boundary layer diagnostic: Regime-dependent turbulence signatures from large eddy simulation and observations, Journal of Geophysical Research: Atmospheres, 131, e2026JD047 347, https://doi.org/10.1029/2026JD047347, 2026.

Kirsch, B., Hohenegger, C., Klocke, D., Senke, R., Offermann, M., and Ament, F.: Sub-mesoscale observations of convective cold pools with a dense station network in Hamburg, Germany, Earth System Science Data, 14, 3531–3548, https://doi.org/10.5194/essd-14-3531-2022, 2022a.

Kirsch, B., Stiehle, B., Löhnert, U., and Ament, F.: Radiosonde profile measurements during FESSTVaL 2021 (Version 00), Dataset, https://doi.org/10.25592/uhhfdm.10279, 2022b.

Kooijmans, L. M. J. and Hartogensis, O. K.: Surface-layer similarity functions for dissipation rate and structure parameters of temperature and humidity based on eleven field experiments, Boundary-Layer Meteorology, 160, 501–527, https://doi.org/10.1007/s10546-016-0152-y, 2016.

Lilly, J. M., Sykulski, A. M., Early, J. J., and Olhede, S. C.: Fractional Brownian motion, the Matérn process, and stochastic modeling of turbulent dispersion, Nonlinear Processes in Geophysics, 24, 481–514, https://doi.org/10.5194/npg-24-481-2017, 2017.

Löhnert, U. and Maier, O.: Operational profiling of temperature using ground-based microwave radiometry at Payerne: prospects and challenges, Atmospheric Measurement Techniques, 5, 1121–1134, https://doi.org/10.5194/amt-5-1121-2012, 2012.

https://doi.org/10.5194/egusphere-2026-4148
Preprint. Discussion started: 31 July 2026

Lüdi, A., Beyrich, F., and Mätzler, C.: Determination of the turbulent temperature-humidity correlation from scintillometric measurements, Boundary-Layer Meteorology, 117, 525–550, https://doi.org/10.1007/s10546-005-1751-1, 2005.

Päschke, E., Becker, C., and Beyrich, F.: Regional-scale vertical fluxes from an optical-microwave scintillometer during FESSTVAL 2021, Dataset, https://doi.org/10.25592/uhhfdm.11980, 2023.

Rose, T., Crewell, S., Löhnert, U., and Simmer, C.: A network suitable microwave radiometer for operational monitoring of the cloudy atmosphere, Atmospheric Research, 75, 183–200, https://doi.org/10.1016/j.atmosres.2004.12.005, 2005.

Seidel, D. J., Ao, C. O., and Li, K.: Estimating climatological planetary boundary layer heights from radiosonde observations: comparison of methods and uncertainty analysis, Journal of Geophysical Research: Atmospheres, 115, D16 113, https://doi.org/10.1029/2009JD013680, 2010.

Sinclair, V. A., Ritvanen, J., Urbancic, G., Statnaia, I., Järvi, L., O'Connor, E., Schneider, T., and Lampilahti, J.: Boundary-layer height and surface stability at Hyytiälä, Finland, in ERA5 and observations, Atmospheric Measurement Techniques, 15, 3075–3103, https://doi.org/10.5194/amt-15-3075-2022, 2022.

Speidel, J., Vogelmann, H., Behrendt, A., Lange, D., Mauder, M., Reichardt, J., and Wolz, K.: The ATMONSYS water vapor DIAL: advanced measurements of short-term variability in the planetary boundary layer, Atmospheric Measurement Techniques, 18, 4923–4948, https://doi.org/10.5194/amt-18-4923-2025, 2025.

Sykulski, A. M., Olhede, S. C., Guillaumin, A. P., Lilly, J. M., and Early, J. J.: The debiased Whittle likelihood, Biometrika, 106, 251–266, https://doi.org/10.1093/biomet/asy071, 2019.

Taylor, G. I.: The spectrum of turbulence, Proceedings of the Royal Society of London. Series A, 164, 476–490, https://doi.org/10.1098/rspa.1938.0032, 1938.

Turner, D. D. and Löhnert, U.: Ground-based temperature and humidity profiling: combining active and passive remote sensors, Atmospheric Measurement Techniques, 14, 3033–3048, https://doi.org/10.5194/amt-14-3033-2021, 2021.

Ward, H. C., Evans, J. G., and Grimmond, C. S. B.: Multi-scale sensible heat fluxes in the suburban environment from large-aperture scintillometry and eddy covariance, Boundary-Layer Meteorology, 152, 65–89, https://doi.org/10.1007/s10546-014-9916-4, 2013.

Weckwerth, T. M.: The effect of small-scale moisture variability on thunderstorm initiation, Monthly Weather Review, 128, 4017–4030, https://doi.org/10.1175/1520-0493(2000)129<4017:TEOSSM>2.0.CO;2, 2000.

Wheelon, A. D.: Electromagnetic Scintillation. I. Geometrical Optics, Cambridge University Press, https://doi.org/10.1017/CBO9780511534805, 2001.

Wulfmeyer, V., Hardesty, R. M., Turner, D. D., Behrendt, A., Cadeddu, M. P., Di Girolamo, P., Schlüssel, P., Van Baelen, J., and Zus, F.: A review of the remote sensing of lower tropospheric thermodynamic profiles and its indispensable role for the understanding and the simulation of water and energy cycles, Reviews of Geophysics, 53, 819–895, https://doi.org/10.1002/2014RG000476, 2015.